



An experimental and modeling study of the thermomechanical behavior of an ABS polymer structural component during an impact test

Hervé Louche, F. Piette-Coudol, R. Arrieux, J. Issartel

► To cite this version:

Hervé Louche, F. Piette-Coudol, R. Arrieux, J. Issartel. An experimental and modeling study of the thermomechanical behavior of an ABS polymer structural component during an impact test. *International Journal of Impact Engineering*, 2009, 36 (6), pp.847. <10.1016/j.ijimpeng.2008.09.007>. <hal-00573075>

HAL Id: hal-00573075

<https://hal.science/hal-00573075v1>

Submitted on 3 Mar 2011

HAL is a multi-disciplinary open access archive for the deposit and dissemination of scientific research documents, whether they are published or not. The documents may come from teaching and research institutions in France or abroad, or from public or private research centers.

L'archive ouverte pluridisciplinaire **HAL**, est destinée au dépôt et à la diffusion de documents scientifiques de niveau recherche, publiés ou non, émanant des établissements d'enseignement et de recherche français ou étrangers, des laboratoires publics ou privés.

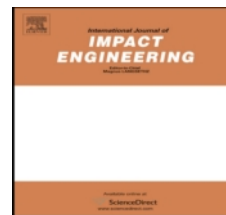


HAL Authorization

Accepted Manuscript

Title: An experimental and modeling study of the thermomechanical behavior of an ABS polymer structural component during an impact test

Authors: H. Louche, F. Piette-Coudol, R. Arrieux, J. Issartel



PII: S0734-743X(08)00233-9

DOI: [10.1016/j.ijimpeng.2008.09.007](https://doi.org/10.1016/j.ijimpeng.2008.09.007)

Reference: IE 1705

To appear in: *International Journal of Impact Engineering*

Received Date: 5 February 2008

Revised Date: 11 July 2008

Accepted Date: 16 September 2008

Please cite this article as: Louche H, Piette-Coudol F, Arrieux R, Issartel J. An experimental and modeling study of the thermomechanical behavior of an ABS polymer structural component during an impact test, *International Journal of Impact Engineering* (2008), doi: 10.1016/j.ijimpeng.2008.09.007

This is a PDF file of an unedited manuscript that has been accepted for publication. As a service to our customers we are providing this early version of the manuscript. The manuscript will undergo copyediting, typesetting, and review of the resulting proof before it is published in its final form. Please note that during the production process errors may be discovered which could affect the content, and all legal disclaimers that apply to the journal pertain.

An experimental and modeling study of the thermomechanical behavior of an ABS polymer structural component during an impact test

H. Louche^(1,*), F. Piette-Coudol^(1,2), R. Arrieux⁽¹⁾, J. Issartel⁽²⁾

^(*) Corresponding author: herve.louche@univ-savoie.fr, Tel: +33 (0) 450 096 568, Fax: +33 (0) 450 096 543

⁽¹⁾ SYMME – POLYTECH' Savoie – Université de Savoie BP 80439, F- 74944 Annecy Le Vieux Cedex, France

⁽²⁾ CTC, 4 rue Hermann Frenkel, 69367 Lyon cedex 07, France

Abstract :

An experimental and modeling study of the thermomechanical behavior of an ABS polymer structural component during an impact test is presented. The structural component was a heel of a woman's shoe made of ABS polymer material reinforced or not by a pin. Kinematics and thermal full field measurement techniques were used to observe the material and structural component during preliminary experimental tensile and impact tests. With the kinematic fields it was possible to identify the stress-strain response, which takes the necking localization into account. Positive volume variations were also observed during these tensile tests, which were associated with the crazing damage mechanisms in this type of polymer. The thermal fields measured during these tests showed high temperature variations (a few K to 25 K) in the zone where strain was localized.

The associated thermal softening, estimated by the stress strain responses at various imposed room temperatures, was taken into account in the Johnson Cook material model. This model was selected because it can easily include the strain, strain rates and temperature effects. A thermomechanical simulation was built. This weak coupled model is based on the assumption of both the adiabaticity of the problem and a fixed ratio (90%) of the local volume plastic power of the heat sources.

The finite element model was restricted to the first impact test. A specific instrumentation of the machine was performed to validate the model. Displacements, linear and angular velocities and impact load were measured. In addition to these local data, kinematics and thermal full field measurements were proposed and provided a rich spatiotemporal database to compare the experimental and numerical results. A qualitative agreement for the strain distribution and an underestimation of about 20% of the impact load was finally obtained by the model.

Key words :

ABS polymer, impact test, kinematics and thermal fields, thermomechanical couplings, finite element model.

1. INTRODUCTION

Polymers are often used in applications where impact resistance is required. In this context, specific polymers such as ABS (acrylonitrile butadiene styrene) have been created with rubber particles in order to increase the toughness. The particles act as craze stabilizers, thereby delaying crack initiation and increasing the strain to failure [1-3]. The deformation of a structural component or a tensile sample during characterization tests can be accompanied by intense strain localization and more or less temperature variations, depending mainly on the material and strain rates [4-8]. However, these characteristics are not systematically taken into account when the material mechanical models are designed [8]. The main reason is that competition between the strain rate hardening and the temperature is hard to characterize in experiments. The tests are supposed to be homogeneous in order to simplify identification. This hypothesis is open to criticism in certain situations. For example, [8] considers that the effect of intrinsic dissipation is significant for polymers as of 10^{-2} s^{-1} . Indeed, the thermomechanical couplings in polymers due to the irreversibilities (viscosity and/or plasticity and/or damage, etc.) generate heat sources (intrinsic dissipation), leading to local rises in temperature. These temperature variations, whose intensity depends on the heat sources and heat conduction problem, can, according to their intensity and the thermal softening of the material, modify its flow and strain rate. In this context of heterogeneous tests, full field measurements (kinematics and thermal), while bringing additional local thermomechanical information (displacements, strains, strain rates, temperatures, dissipation, etc.) must be exploited to improve the identification of material models in sample tests and the validation in structural component tests. Moreover, few thermomechanical modeling studies have been conducted during impact test loading [9-14]. Among these, the most advanced was the DSGZ model proposed by [10]. Their phenomenological thermoelastoviscoplastic model, defined by eight parameters, took into account the loading mode, through a ponderation of the hydrostatic pressure. Implemented with a Vumat program in the Abaqus/Explicit software, the resolution was conducted using a weak coupled adiabatic thermomechanical problem, including a fixed ratio (90%) of plastic power converted into heat. The model was then applied to a multiaxial impact behavior on a glassy ABS polymer structural component [11, 12].

The objectives of this paper are: 1) to present the different steps of a thermomechanical study of an industrial impact test on an ABS polymer structural component; 2) to show how thermomechanical field measurements improve the modeling of this study.

The structural component is a heel of a woman's shoe. This kind of product and its commercial success closely depend on shoe fashion. Industrial stakeholders have to propose competitive products at the right time. Numerical tools, like structural component finite element simulation, can help this industry to optimize their products, mainly through geometry and material choices, and reduce the design time. A practical impact test is currently used to validate the design choices. This test involves using a pendulum. The base of the heel is fixed, impacts are applied at the end of the

heel in the normal direction along the principal axis. To be validated, the heel has to withstand a number N of impacts, typically $N=300$. This practical test can be critical for some heel solutions and, in these cases, can substantially increase the design time. A numerical model of the real impact test is thus required in order to optimize the design choices (mainly the geometry and the material) of the heels and to reduce the design time. The present study relates only to a slanted heel type, without or with a reinforcement pin, and made by plastic injection with an ABS material.

The model used in this study was restricted to the "first impact". This choice was based on: (i) the complexity of the deformation mechanisms, with damage due to crazing during dynamic loading; (ii) high dispersion in the number of cycles at failure. Even if the rupture of the structural component happens at the end of some impacts (classically a few tens), the first impact is often very critical for certain geometrical designs. The model of the first impact is thus essential for continuation of the design project. The prediction, beyond this first impact, of the structural behavior is complex and would require the development of oligocyclic fatigue models.

The paper is organized as follows: in Section 2 we describe the thermomechanical tensile test experiments used to identify the material constitutive model described in Section 3. A specific instrumentation of the pendulum developed to validate the model is presented in Section 4. We then present the finite element model in Section 5 and the main results in Section 6.

Complementary information on this study is available in [15].

2. TENSILE TEST EXPERIMENTS

The tested ABS was a commercial polymer (Novodur P2M Grade). The specimens used for identification were flat, with a reduced gauge length of $L \cdot I \cdot e = 80 \cdot 10 \cdot 4 \text{ mm}^3$. Injected at one injection point, they were made under process conditions close to those used to make the structural component (via injection).

During the impact, the structural component was primarily subjected to bending, thus inducing loading of traction and compression. The ideal would thus be to carry out compression and tensile tests at the same time. However, compression tests are difficult to perform. They require cylindrical test specimens and a restrictive hypothesis to estimate the stress. Moreover, only tensile tests were conducted because the traction state was more severe for crazing development. In order to study ABS under the same conditions (strain rates and temperatures) as during the impact test, tensile tests at various strain rates and temperatures were thus carried out. A large strain rate range was used, from quasi-static (10^{-3} s^{-1}) to higher values (2 s^{-1}), which can be reached at the time of the impact. Tests with imposed temperature were carried out for temperature values ranging from 20°C (room temperature) to 60°C .

Global measurements

Global load displacement curves, during tensile tests, are plotted in Figure 1. In each situation (strain rate or imposed temperature) three samples were tested, the results presented in this figure are representative of these tests.

An environmental chamber was used for tests at a “fixed” imposed temperature. Figure 1a shows the high sensitivity rate of the material, with an increase in the yield stress and plastic flow with the strain rate. An increase of the Young modulus with an increase of the strain rate can also be noticed. This phenomenon can be associated to viscous effects in this apparent “elastic” loading. Such dependence was not taken into account in the following of this work. Conversely, thermal softening is observed in Figure 1b for three temperature values, at a constant imposed strain rate. The strain rate hardening and thermal softening effects for the yield stress (engineering stress) is plotted in Figure 1c. This yield stress pattern, associated with the beginning of the macroscopic irreversibility of the material, will be used later for identification of the material constitutive model.

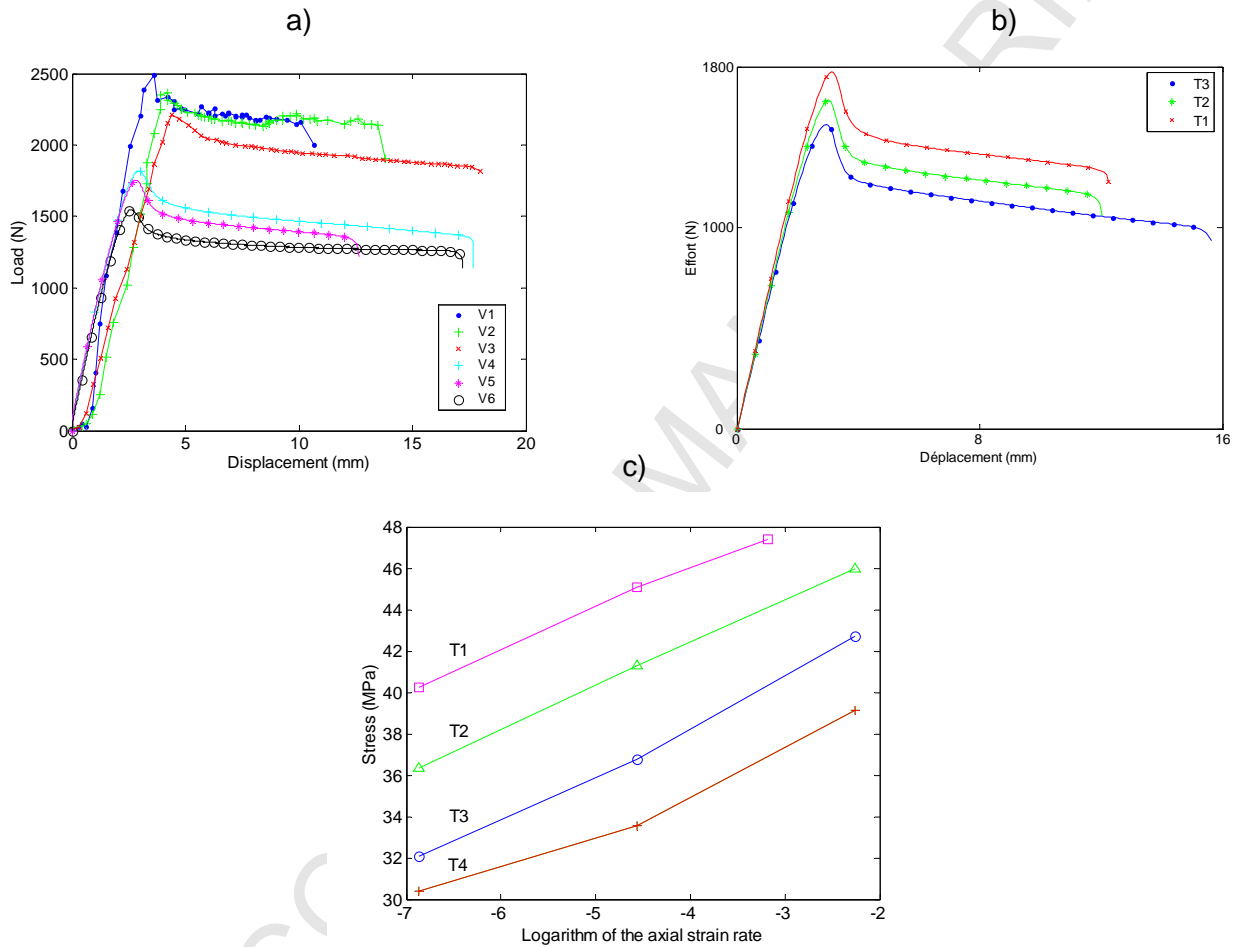


Figure 1: Global mechanical response for: a) various strain rates ($V_1=2 \text{ s}^{-1}$, $V_2=1 \text{ s}^{-1}$, $V_3=0.2 \text{ s}^{-1}$, $V_4=3.10^{-2} \text{ s}^{-1}$, $V_5=1.10^{-2} \text{ s}^{-1}$, $V_6=1.10^{-3} \text{ s}^{-1}$), b) various imposed ambient temperatures ($T_1=40^\circ\text{C}$, $T_2=50^\circ\text{C}$, $T_3=60^\circ\text{C}$), at 0.1 s^{-1} . c) Yield stress vs. strain rates, for various imposed room temperatures ($T_1=27^\circ\text{C}$, $T_2=40^\circ\text{C}$, $T_3=50^\circ\text{C}$, $T_4=60^\circ\text{C}$).

Kinematical fields

The displacement fields $\mathbf{u}=(u_1(x_1, x_2), u_2(x_1, x_2))$, where x_1 and x_2 are respectively the axial and transverse position, were obtained using a digital visible camera (Hamamatsu, 1280×1024 pixels, maximum sampling rate 9 Hz, ambient lighting) and a digital image correlation (DIC) processing (7D[®] software, see [16, 17]). This correlation approach can

be used to measure strain fields, deduced from the displacement fields, from 0.01% to 300%. The displacement accuracy of the DIC approach was typically about 0.01 pixels for deformations under 5%, but this value depended on many parameters, e.g. image quality, strain gradient and the order of the transformation describing the local deformation. The grey level interpolation chosen in the software was bicubic and the strain fields were computed on the basis of bilinear expression of the spatial displacement distribution. The optimisation method used to find the minimum correlation function was a gradient method. With the above characteristics, and a correlation pattern of 12x12 pixels, errors under 0.01 pixels were obtained in the displacement fields for: a) rigid body motions imposed on synthetic images, and b) for homogeneous deformation imposed on synthetic images [17]. All the 7D[®] strain results were obtained using the Green-Lagrange strain tensor \mathbf{E} . In the following, the axial component E_{11} of this tensor or the Logarithmic axial strain ε_{11} will be used, as determined from the local axial displacement u_{11} (expressed in the initial configuration).

For each test, it was then possible to study the strain fields and to specifically analyze localization phenomena and volume variations.

Strain localization detection

The measured kinematic fields enabled detection of the position and intensity of the strain localization (Figure 2). For the ABS polymer tensile tests, the localization was associated with necking, which was located in a fixed position at all times (here close to point 1 plot in Figure 2a). Knowledge of the kinematics fields at all acquisition times allowed us to take the localization into account [7,18]. It was obtained while focusing on the local stress strain response of measurement points centered on cross-sections distributed along the axial direction of the sample (Figure 2-a). The stress was the “true stress” obtained with the local axial strain measured at these points. The local mechanical responses showed that the sample behaved like a structural component. The deformation was only elastic in certain parts of the sample remote from the necking zone. On the other hand, those located in the necking zone underwent very high unrecoverable deformations of up to 65% (Figure 2-c). The incompressibility assumption used to calculate the “true stress” will be discussed hereafter. Moreover, it was supposed, which is no longer true when necking is strongly localized, that the stress state remained uniaxial and homogeneous on the cross section. In the following, the stress-strain response used to derive the material behavior will be identified using the local strain, measured in the necking area where higher strain values were obtained.

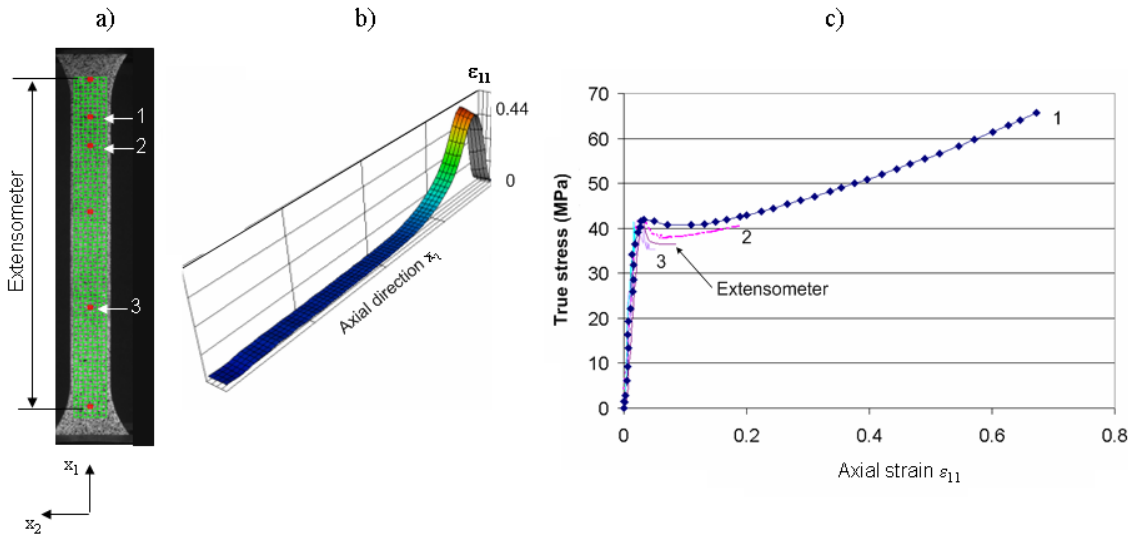


Figure 2: a) Photograph of the sample with the virtual grid, the position of the three local points and the virtual extensometer, b) logarithmic axial strain field ϵ_{11} observed for a global displacement of 9 mm, at a strain rate of 8.10^{-4} s^{-1} , c) Local response (true strain and true stress) obtained in the three different points of Figure a). The mean axial strain given by the extensometer is 0.09, instead of the local value of 0.65 given by the strain field analysis.

Volume variation study

Due to crazing phenomena, deformation of the ABS polymer was usually accompanied by a volume variation. The main mechanism associated with this damage phenomena was cavitation near rubber particles, which generates volume variation [5,6]. This could be estimated by the formula $\epsilon_V = \ln\left(\frac{\Delta V}{V_0}\right) = \epsilon_{11} + \epsilon_{22} + \epsilon_{33}$ where ϵ_{ii} is the logarithmic strain in the principal direction i , $i=1$ is the loading axis. Using the measured kinematic fields and assuming strain homogeneity in the transverse direction ($\epsilon_{22} = \epsilon_{33}$), it was then possible to plot the volume variation patterns (see Figure 3a). The volume variation increased from the very start of the plastic range, which was not the case for all the polymers (see [6] for example).

In our study strains in 22- and 33-directions were equalled. As shown in Fig2a, the observed plane by the camera is (1,2), so it's was not possible to measure the ϵ_{33} strain field. This should be possible with a second camera oriented in the 3 direction or using a mirror oriented with an angle of 45° in order to reflect the image of the “thickness side” of the sample in the unique camera.

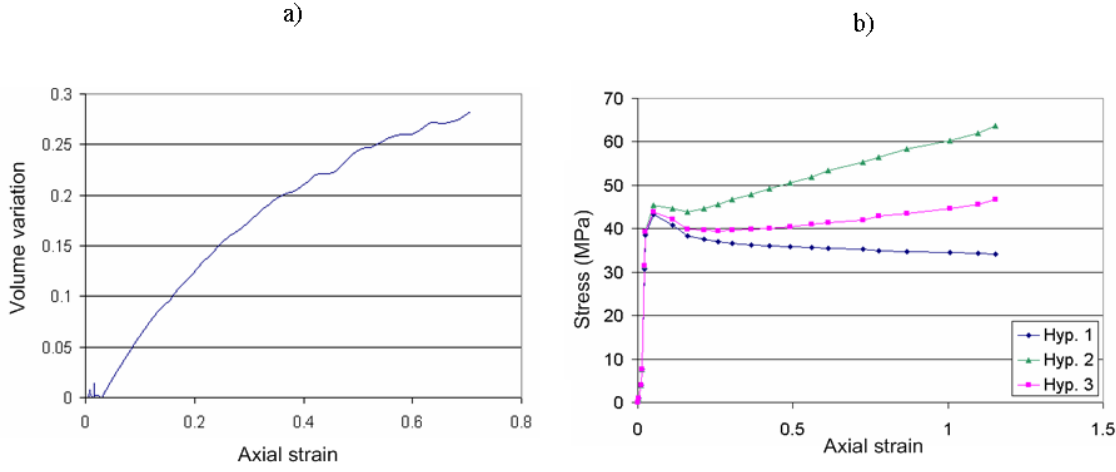


Figure 3: a) Volume variation measured during a tensile test at 8.10^{-4} s^{-1} , b) Stress strain responses, for the three hypotheses, at a strain rate of 8.10^{-3} s^{-1} .

These volume variation observations must be taken into account to calculate stresses. Indeed, the passage of the total response (load, displacement) to the local responses (stress, strain) can be obtained by correcting or not the cross section of the sample. Three assumptions are classically used:

- Hyp. 1: engineering stress, without volume correction: $\sigma_{nom} = \frac{F}{S_0}$
- Hyp. 2: true stress, corrected section with the incompressibility hypothesis: $\sigma = \frac{F}{S} = \sigma_{nom} \cdot e^{\varepsilon_{11}}$
- Hyp. 3: true stress, corrected section with volume variation [6] : $\sigma = \frac{F}{S} = \sigma_{nom} \cdot e^{-2\varepsilon_{22}}$. This formula is

based on the assumption that the strain in the transverse ε_{22} and thickness ε_{33} directions were equal.

The mechanical responses were very different (Figure 3b). The elastic part was the same, then a difference appeared after the yield point. The hypothesis of deformation with incompressibility implied a higher flow stress value. The response obtained with hypothesis 3 was located between the two other responses. This hypothesis was based on the cross section variations obtained only by external observations: strains ε_{22} and ε_{33} measured on the external surfaces. However, crazing damage due to porosity development around rubber particles may decrease the effective cross section area. Such a mechanism was compatible with the volume variation measurement given in the previous part. A better stress estimation could be obtained with a damage model, and the mechanical response would be located between the responses given by hypothesis 2 and 3.

In this work, a thermoelastoviscoplastic model, assuming volume conservation, was used to simulate the mechanical behavior of the impacted structural component.

Thermal fields

The temperature field T recorded during a test was obtained with a fast multidetector infrared camera (CEDIP Jade III MW, 145 Hz maximum frame rate). This camera had a noise level of less than 20 mK, and a spatial resolution of 320×240 pixels. The spatial resolution (pixel size), which depends on the focal distance adjustment, was estimated to be close to 0.25 mm for the carried out tests. Prior to testing, the surface of the tube was coated with a highly emissive paint in order to obtain blackbody properties compatible with the calibration law of the camera obtained in the same conditions. Moreover, temperature results were always note relative to an equilibrium room temperature, which led to a temperature variation accuracy of less than 0.1°C .

The temperature variation was measured locally on one face of the sample (Figure 4a). The temporal temperature variation patterns at three different spatial points showed the thermal history of different zones of the sample used for material identification (Figure 4b). This test, which was performed at high strain rate (mean value of $4,5 \cdot 10^{-2} \text{ s}^{-1}$), revealed surface temperature variations of up to 26°C in the necking zone. For zones far from the necking localization, the test could be considered as isothermal (temperature variations were less than 1°C).

On materials with low thermal diffusion, temperature variations during a tensile test can locally reach a few degrees and consequently modify the behavior of the material [4, 8]. As previously noted for the kinematic measurements, it would be necessary to take the temperature heterogeneity into account in the identification of the material constitutive model. In addition to the irreversibilities detection and the quantification of the temperature variations, the thermal fields also make it possible to establish energy balances [19]. Such assessments, which are not presented here, could highlight the fraction of mechanical energy which was converted into heat, i.e. a parameter fixed constant at the time of the simulations presented hereafter.

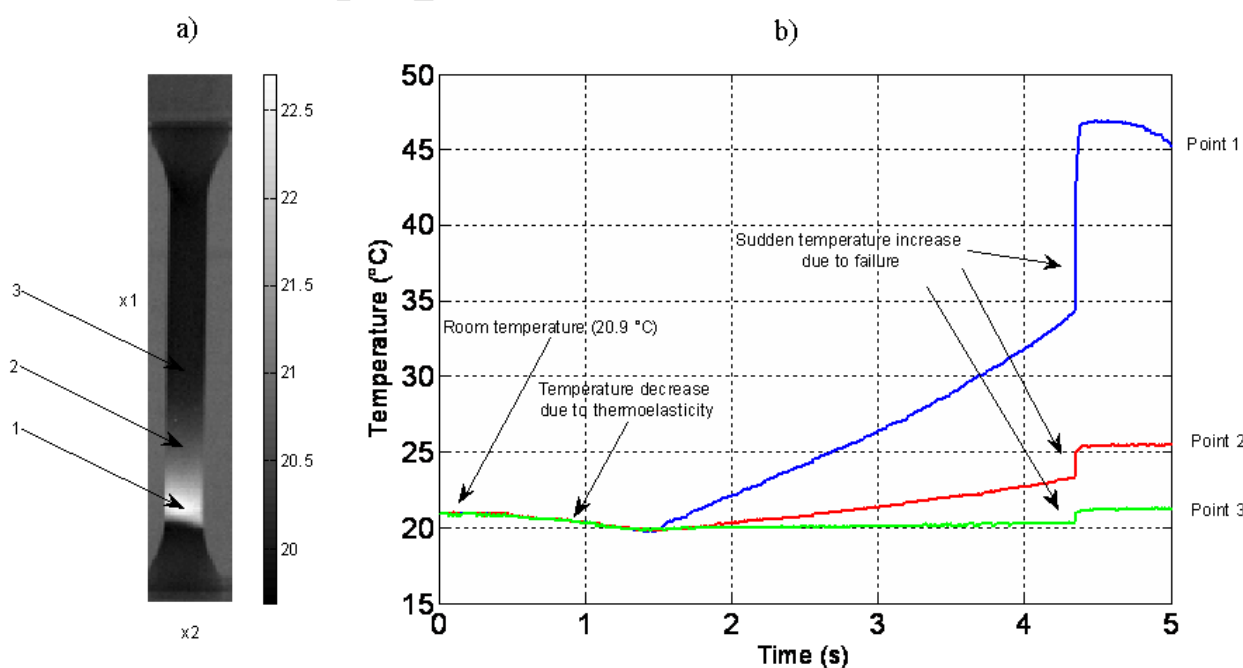


Figure 4: a) Thermal field, at a fixed time ($t=2s$, see Figure b), observed during a tensile test at a strain rate of $4.5.10^{-2} s^{-1}$, showing a localization at the bottom of the sample (point 1). b) Temporal variations in the temperature at the three spatial points of the previous figure. The high temperature jump ($+26^{\circ}C$) observed at point 1, at time 4.3 s, is associated with intense dissipation in the necking zone during failure. In the two other points, the temperature increase is mainly due to thermoelasticity linked to elastic spring back.

3. MATERIAL CONSTITUTIVE MODELING

Johnson Cook model

In this study, the material constitutive model was developed on the basis of tensile tests. Other tests, like compression tests, which are harder to interpret, could ultimately supplement this identification.

The use of finite element software for this impact test study on a structural component determined the choice of material constitutive model. Among the possible models available in this software, none could simultaneously take the damage, strain rate sensitivity and temperature into account. We thus decided to use elastoviscoplastic models of behavior that can take thermal softening into account.

In this context, the Johnson Cook model was selected:

$$\bar{\sigma} = \left(A + B \bar{\varepsilon}^{pl n} \right) \left(1 + C \ln \left(\frac{\dot{\bar{\varepsilon}}}{\dot{\bar{\varepsilon}}_0} \right) \right) \left(1 - \hat{T}^m \right), \quad (1a)$$

$$\text{for } T < T_{transition} \text{ and } T > T_{melting} \text{ then } \hat{T} = 0, \quad (1b)$$

$$\text{for } T_{transition} < T < T_{melting} \text{ then } \hat{T} = \frac{T - T_{transition}}{T_{melting} - T_{transition}}, \quad (1c)$$

where $\bar{\sigma}$ is the equivalent stress, $\bar{\varepsilon}^{pl}$ is the equivalent plastic strain. The first term of the model describes the plastic behavior of the material, parameter A represents the yield stress, B and n are linked to the plastic flow. The second term reflects the strain rate sensitivity. The last term corresponds to the thermal softening of the material. Below the transition temperature ($T_{transition}$), the yield stress was unchanged. Thermal softening appeared at temperatures ranging between the transition temperature and the melting temperature ($T_{melting}$). The yield stress was null beyond this temperature. Finally, m characterizes the extent of thermal softening.

The model parameters were identified according to the experimental results of the tensile tests at various strain rates and temperatures. The hardening parameters A, B and n of the Johnson Cook model were identified on the basis of various tests at room temperature.

The temperature sensitivity parameter m was identified during tensile tests at imposed temperatures between $T_{transition}$ and $T_{melting}$, while the strain rate of $\dot{\bar{\varepsilon}}_0$, m was obtained by the equation:

$$m = \frac{\ln\left(1 - \frac{\bar{\sigma}}{A + B\varepsilon^{nl^n}}\right)}{\ln\left(\frac{T - T_{transition}}{T_{melting} - T_{transition}}\right)} \quad (2)$$

The identification of m was then achieved at the yield stress, at different temperatures (40°C, 50°C and 60°C) in the various tests, and a mean value of m was finally chosen.

The identified values of the eight model parameters are indicated in the Table 1 below.

The strain rate sensitivity parameter C was identified in the strain rates range [$V4=10^{-3} \text{ s}^{-1}$, $V6=3.10^{-2} \text{ s}^{-1}$]. This range was limited to 3.10^{-2} s^{-1} because it was not possible to measure the strain fields above 3.10^{-2} s^{-1} , the visible images were too fuzzy. An example of the identified stress strain curves for the two strain rates $V4$ and $V6$ are plotted in Figure 5.

A	B	C	m	n	$T_{transition}$	$T_{melting}$	$\bar{\sigma}_0$
39 MPa	48 MPa	0.053	0.879	1.5	300 K	513 K	8.10^{-4} s^{-1}

Table 1 – Identified values of the Johnson Cook model parameters

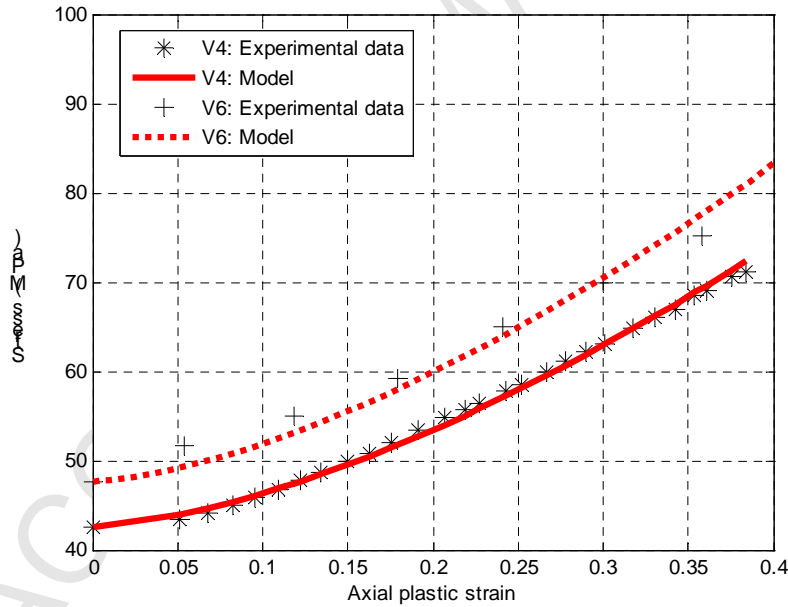


Figure 5: Identification of the Johnson Cook model. Comparison of the stress-strain response given by the model and by the experimental results for two imposed strain rates: $V4=10^{-3} \text{ s}^{-1}$ and $V6=3.10^{-2} \text{ s}^{-1}$.

Validation in a tensile test

Experimental and numerical simulations of a tensile test were carried out on a notched sample (Figure 6a) in order to locate necking at the center of the specimen. Thermal variations in the sample were calculated using a thermo-mechanical model based on the adiabaticity hypothesis, compatible with the thermal diffusion of the material and the

test duration. The heat sources used in the heat diffusion equation were fixed, i.e. 90% of the local plastic power. The specific heat of ABS, provided by the manufacturer, was $1500 \text{ J Kg}^{-1} \text{ K}^{-1}$, the volume mass $\rho=1050 \text{ Kg m}^{-3}$ and the thermal conductivity $k=0.17 \text{ W m}^{-1} \text{ K}^{-1}$.

Only half of the geometry was chosen for the numerical model (Figure 6b). Solid elements (bricks) were used, with a higher density of elements in the sample medium (Figure 6c). One side of the sample was embedded, the other was connected to a mobile part in order to impose the displacement. This one was gradually carried out to avoid elastic impact at the beginning.

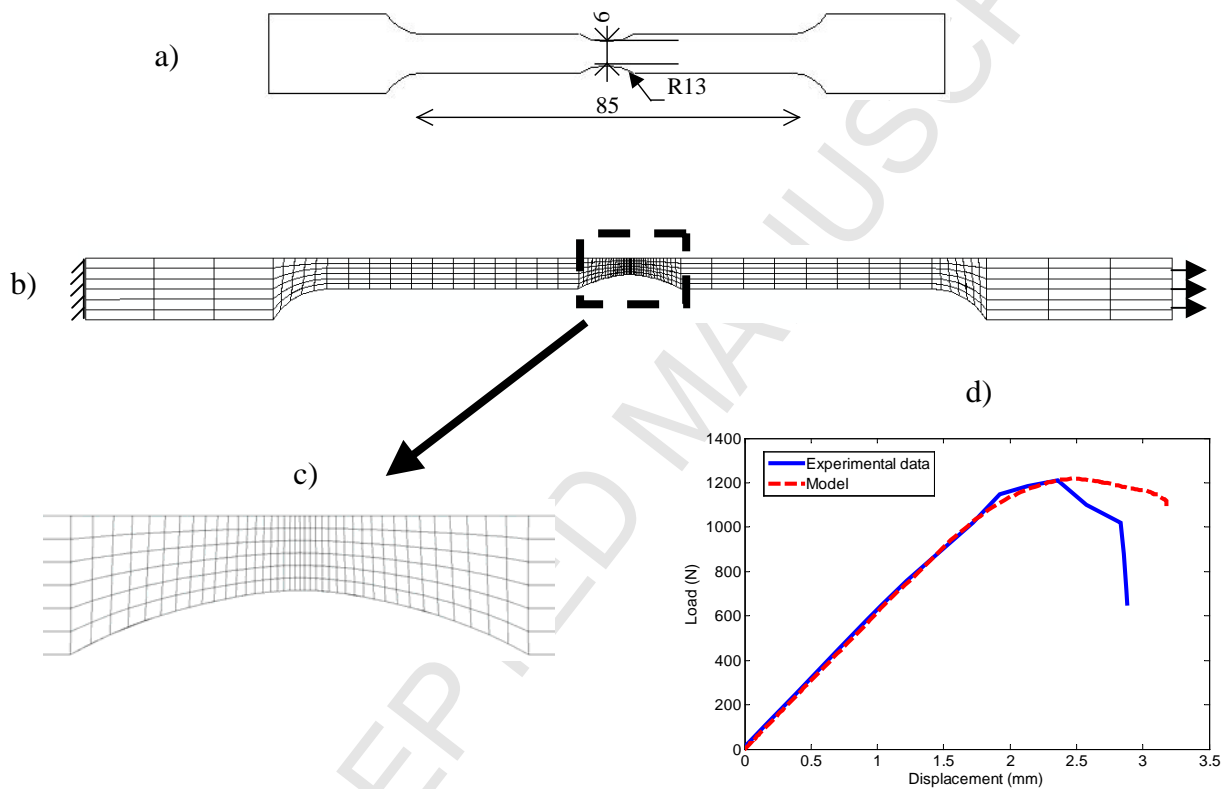


Figure 6: a) Geometry of the notched specimen. b) Global view of the mesh. c) Close-up of the mesh in the notched part. d) Comparison of the model and experimental results, under imposed strain rate (4.10^{-2} s^{-1}) and room temperature (27°C) conditions.

The global load displacement response is plotted in Figure 6d. Simulated and experimental responses were equal until the yield stress. Then, since damage was not taken into account in the model, the apparent experimental softening behavior was not well reproduced, i.e. the calculated loads were higher than the measured loads.

The local calculated and observed results were compared just before necking (Figure 7), at a global displacement of about 3.18 mm and an imposed strain rate of 2.10^{-2} s^{-1} .

Measurement of field kinematics carried out with the 7D[®] software showed a strain localization in the center of the sample (Figures 7a, b). The logarithmic strains reached 30% in the notched zone, while the remainder of the sample remained weakly deformed. The same distribution was obtained for the calculated strain fields, with a maximum of 32% of the logarithmic strain at the center of the sample (Figure 7c).

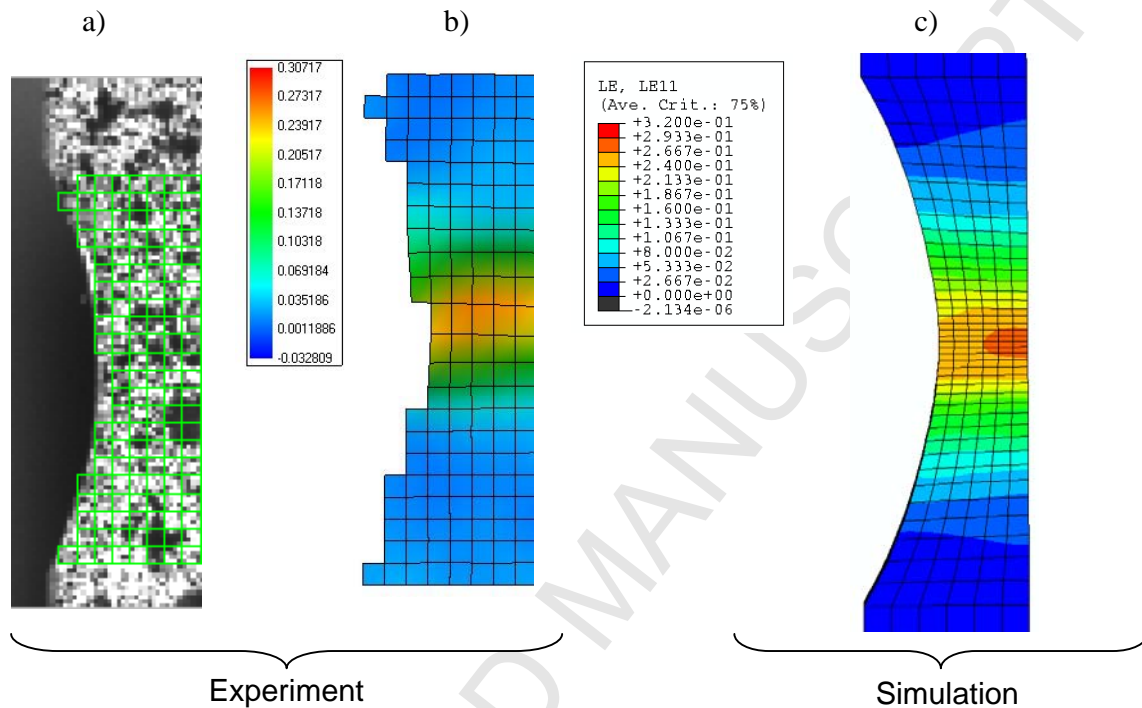


Figure 7: a) Digital image of the notched zone, with the virtual grid used in the 7D[®] DIC software. b) Experimental and c) simulated fields of the axial logarithmic strain in the notched zone.

For the same tests, temperature fields were simultaneously recorded with the infrared camera. An example of the measured temperature field is given in Figure 8a, with an axial and transverse profile showing the marked increase of temperature in the reduced section (Figure 8b). This field was recorded just before failure. The maximum temperature reached was about 43°C. This value represented a temperature variation of +17°C compared to the room temperature (26°C). However, it corresponded to the heating on the sample surface, whereas the heating within the sample was certainly higher. Heat diffusion along the sample axis was very weak in the ABS material, it covered only a length of 20 pixels (about 2 mm).

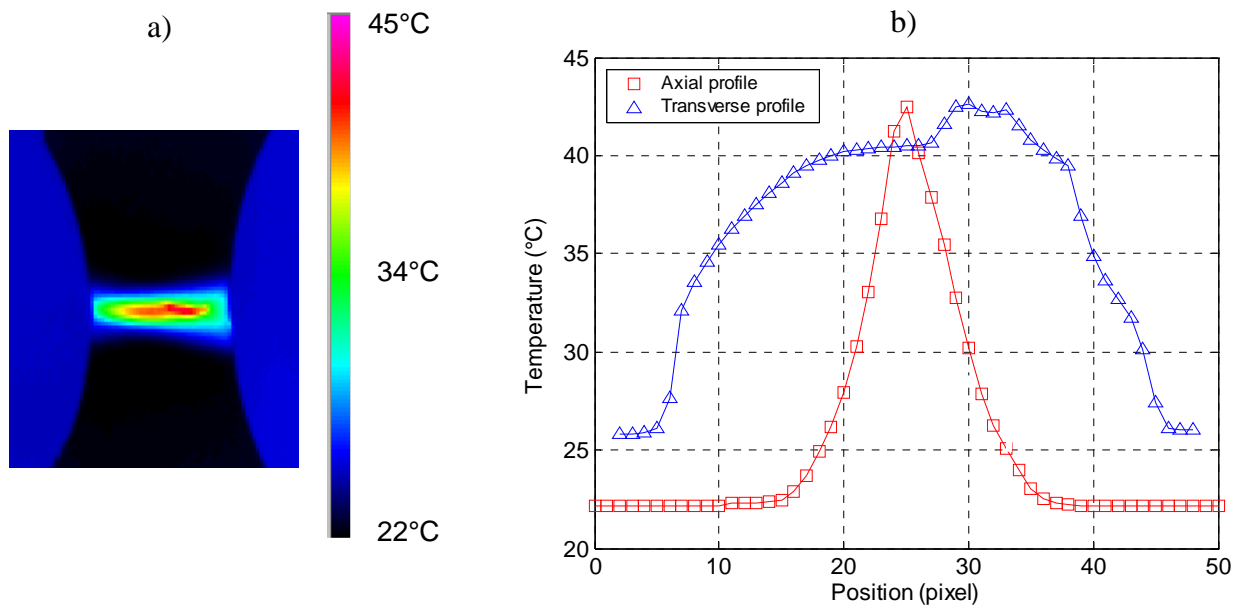


Figure 8: Tensile test at $2 \cdot 10^{-2} \text{ s}^{-1}$. a) Temperature field measured in the notched zone, just before failure. b) Axial and transverse temperature profile (central column and central line of the previous figure)

Temperature variations calculated with the Johnson Cook model are presented in Figure 9. These variations were maximal at the core of the sample. However, the values obtained, i.e. about $+8^\circ\text{C}$, were lower than the experimental values ($+17^\circ\text{C}$). A study of the mesh sensitivity was conducted and showed a mesh independence of the results. The maximum temperature variations at the sample core were limited to $+8^\circ\text{C}$. Two reasons could explain such an under-estimation of temperature variations. The first concerns the phenomenological character of the Johnson Cook model. Indeed, this model was unable to account for dissipative mechanisms of damage phenomena which were experimentally detected with the volume variation. The second concerns the simplified expression of the heat sources, i.e. assumed to be a fixed ratio (an arbitrary value of 90%) of the local plastic power. A more detailed expression of the heat sources, e.g. in the thermomechanical framework of internal variables, should be able to establish a balance between dissipated power and thermomechanical couplings [19].

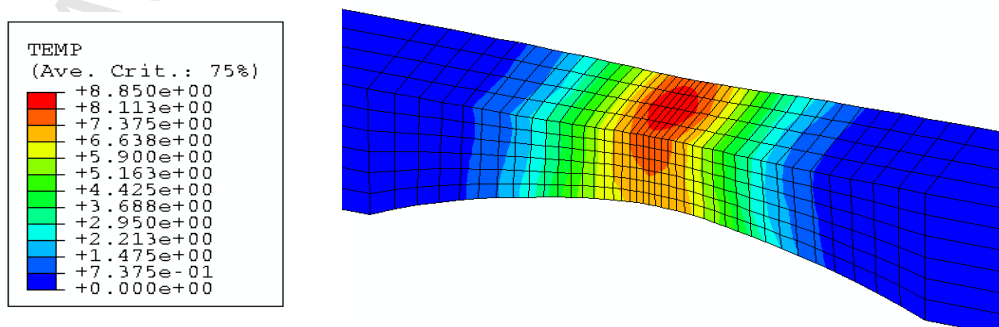


Figure 9: Temperature variations (K) calculated by the Johnson Cook model during a tensile test on a notched specimen.

4. INSTRUMENTATION OF THE PENDULUM

Machine

An uniaxial impact test was conducted with a pendulum machine (Figure 10a). A mass of 1 kg, placed 0.5 m from the rotation axis, imposed (by gravity) rotation of the clapper and displacement of the striker. This latter struck the polymer structural component so that the impact occurred on the vertical plane of the clapper and in the normal direction with respect to the main axis of the structural component (Figure 10b). The machine was equipped with a driving system and a clutch to enable repetition of the impacts. The frequency usually used was 30 impacts per minute, i.e. a frequency of 0.5 Hz (Figure 11a). The base of the structural component was embedded in an aluminum alloy at low melting point (Figure 11b).

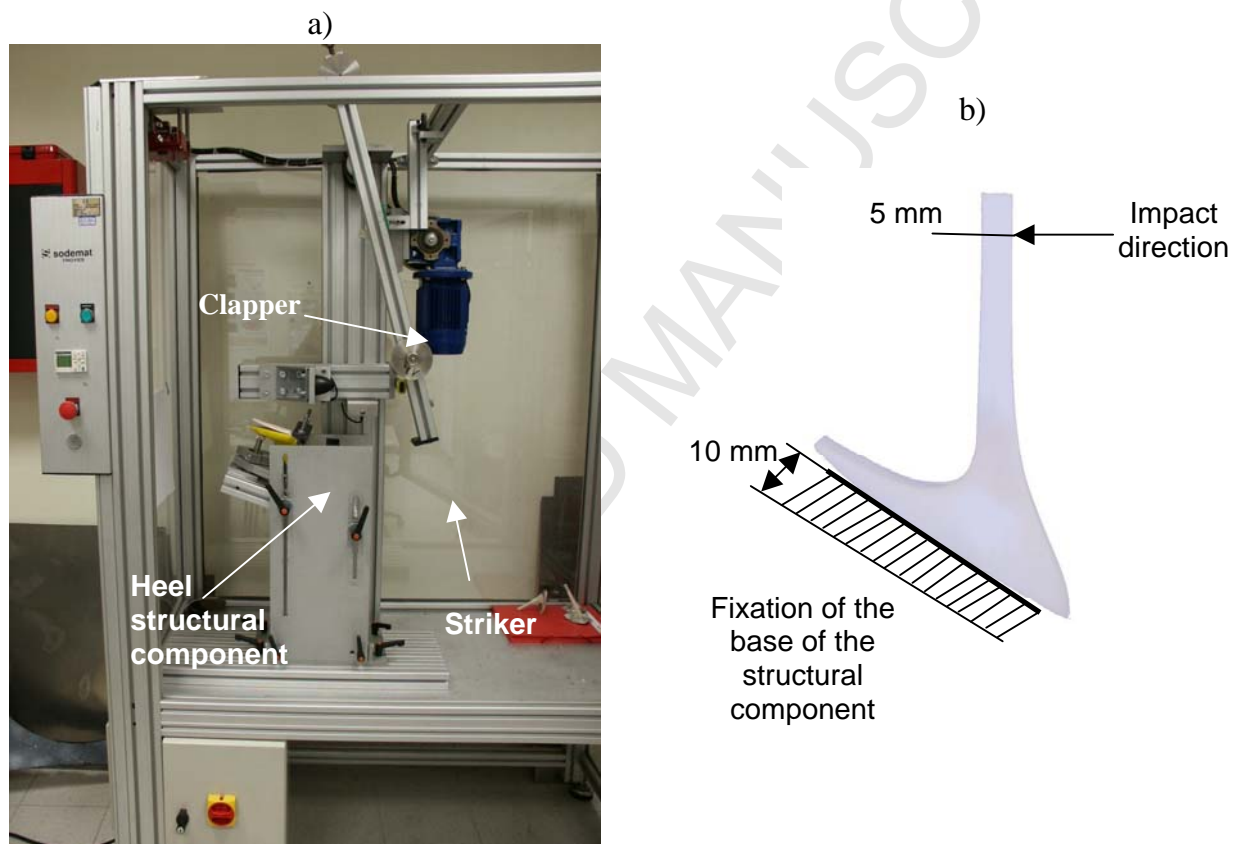


Figure 10: a) Pendulum impact test machine, b) Scheme of the support and load conditions applied to the heel structural component.

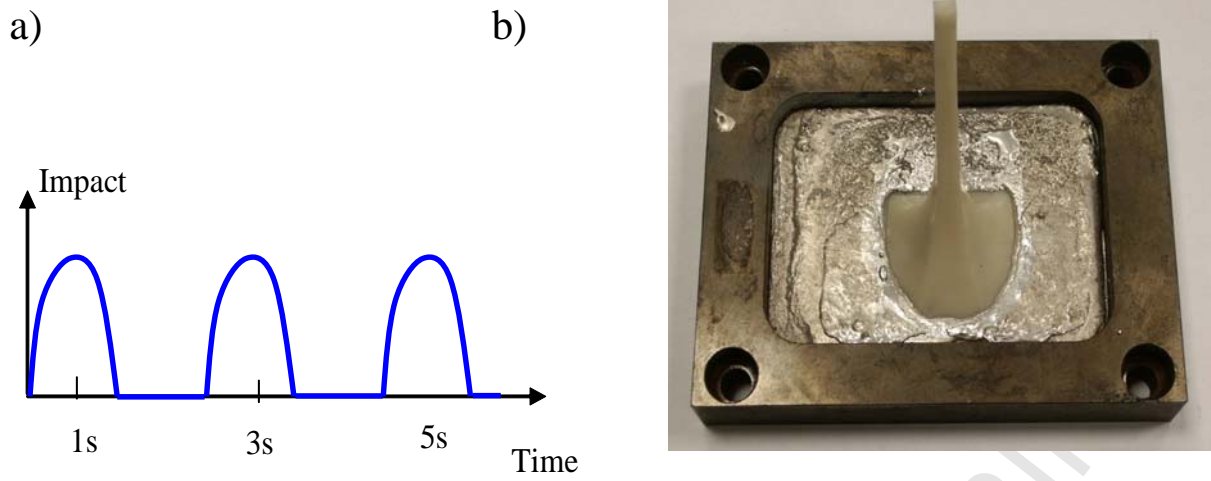


Figure 11: a) Scheme of temporal variations in loading. b) Slanted heel structural component embedded in a low melting point alloy.

Measurements

The modeling of this impact test complied with the characteristics of the machine in order to obtain results close to the real situation. Instrumentation of the testing machine was thus carried out in order to obtain experimental data to validate the model.

Local measurements

Generally, the displacement and load were measured, and this information was obtained through various sensors. In this study, we chose a method based on three types of sensor: a piezoelectric load sensor (PCB 208C04), a piezoelectric accelerometer (Kistler, 500 g) and a gyroscope. We thus measured, respectively, the impact load, the acceleration of the striker and the angular velocity of the clapper (Figures 12a, b). Finally, with the two last sensors it was possible, by time integration, to measure the displacement of the striker and the angular position of the clapper, respectively. An example of a load signal during an impact, with an horizontal initial position of the clapper (angle 90° from the vertical position), is plotted in Figure 12c. Other techniques to measure the load are available, [20,21] used strain gauges stuck on the striker.

The linear velocity during the impact was obtained by integration of the horizontal acceleration γ .

$$V(t) = V_0 + \int_0^t \gamma(t).dt . \quad (3)$$

The constant V_0 , corresponding to the linear velocity just before the impact, was estimated with the angular velocity given by the gyroscope. After various tests, the angular velocity before the impact was estimated at 2.1 rad.s^{-1} , which corresponded to $V_0 = 1.46 \text{ m.s}^{-1}$.

The displacement of the structural component in the impact zone during the impact was obtained by a double time integration of the acceleration. Other experimental techniques can be used to measure displacements at the time of the impact tests, e.g. techniques based on optical lasers are available [0] but more expensive to implement.

A value of 0.73 kg.m^2 for the inertia of the clapper was estimated using CAD software to model the geometry. It was possible to estimate the energy (kinetics) of the impact (1.61 J) with this value and the angular velocity. Due to the friction in the kinematics chain of the clapper, we noted that the value of the impact energy was markedly inferior to the energy (potential) of a perfect machine (5 J).

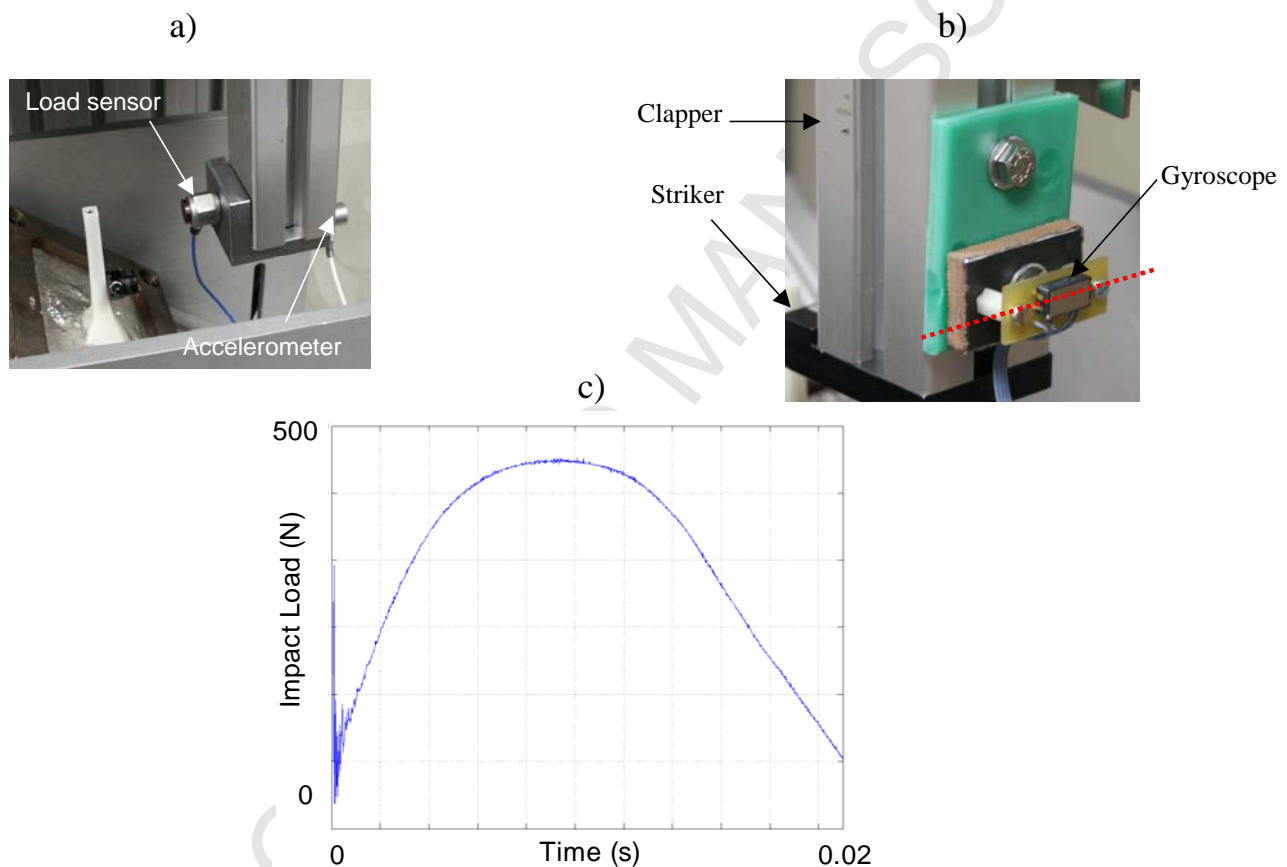


Figure 12: Instrumentation of the machine. a) close-up showing the load sensor used to measure the impact force. b) Close-up of the gyroscope, fixed in the clapper, used to measure its angular velocity. c) Impact load response measured during an impact test at 90° on a slanted heel with a pin.

The permanent displacement of the end of the structural component during repetition of the impact was also used to validate the model. This displacement was measured with the 7D[®] DIC software using sticky labels of random gray levels (Figure 13). Pairs of recorded images, at the initial stage and after an impact, were analyzed by the software to estimate the displacement after impact. Only the horizontal displacement component at the center point of the upper

sticky label is reported here. Figure 13b also shows a damage zone (called "swiveling zone"), close to the support, where crazing phenomena took place. For this type of structural component, this zone was the future site of failure after repeated impacts.

Images were taken after the first impact and then after every ten impacts, when the clapper was up and oscillations of the heel damped. The tests were repeated and allowed us to compile a database on horizontal permanent displacement of the structural component during the impact test. An example of the displacement patterns is plotted (Figure 14a) for various tests carried out on 10 of the same type of heels (slanted and reinforced by a pin). Displacements increased very quickly as of the first 10 impacts, and then the variations leveled off and decreased. The dispersion of the results was weak at the beginning of the test, but progressively increased with the repetition of the impacts, with variations of up to 7 mm for the same number of impacts. We noted that only three heels, among the 10 tested, reached the required 300 impacts.

Due to the difficulty in modeling the repetition of impacts, as well as the substantial dispersion of the experimental results, we were limited to studying and simulating only one impact at a time. In order to be able to compare the simulation results with the experimental results, we observed permanent displacement associated with the first impact. We noted a mean value of 1.1 mm and a standard deviation of 0.19 mm (Figure 14b).



Figure 13: Digital images used by the DIC software to estimate displacements at the end of the structural component:

a) initial state, b) after 140 impacts, with an indication of the measured displacement.

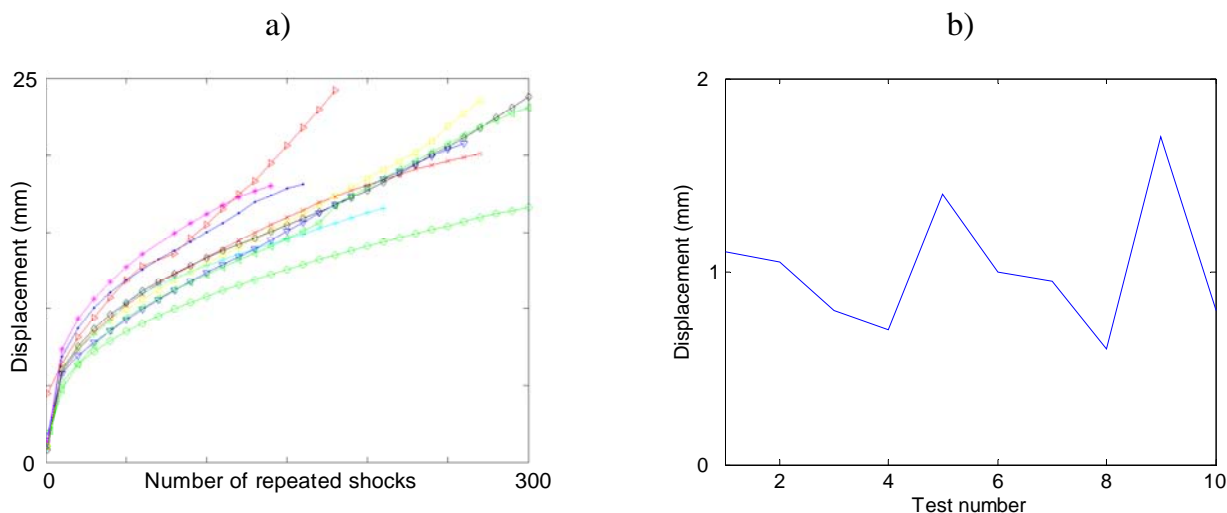


Figure 14: a) Variations, with the number of repeated impacts, in the permanent displacement measured at the end of the structural component; the 10 curves are associated with the 10 heels tested. b) Permanent displacement after the first impact, for the different tests.

Full field thermal measurements

In order to gain insight into the extent thermomechanical couplings in the studied polymer (ABS), we monitored temperature changes during an impact test on various heels. Using an infrared camera, surface temperature variations of the structural component and temperature patterns during impacts in the heating zone were studied. These observations revealed critical zones in the structural component, which corresponded to the zones of failure in the heel. Such zones differed according to the heel geometry.

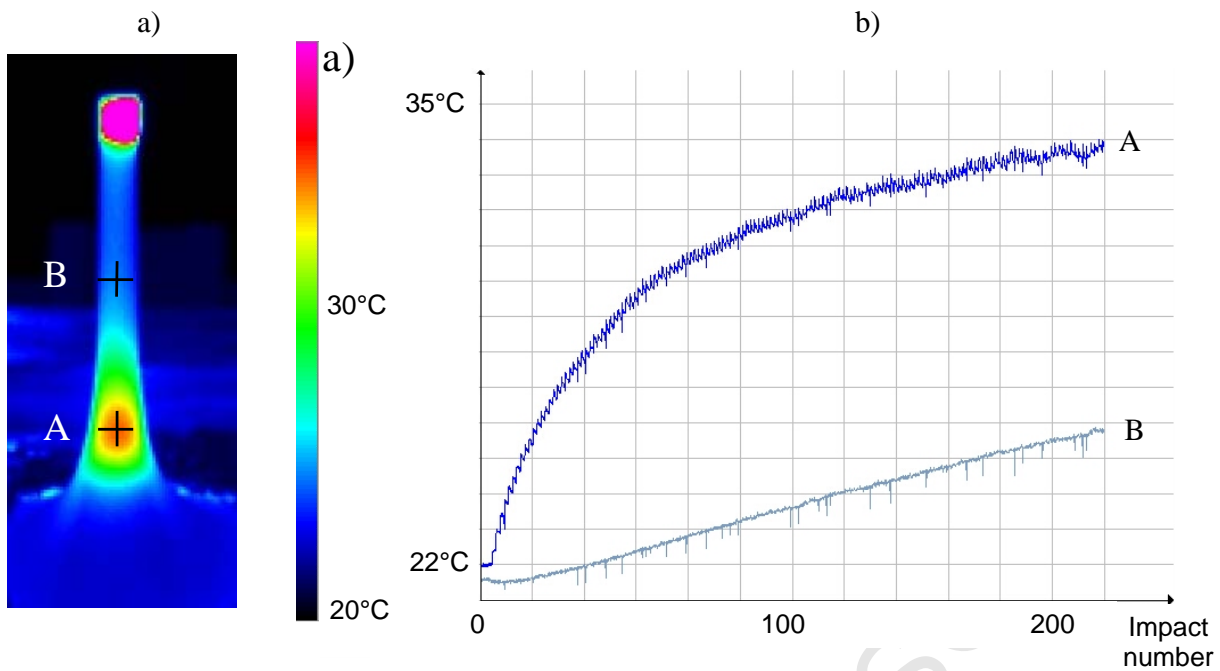


Figure 15: Temperature field measurement in a slanted heel. a) Temperature field after 208 impacts. b) Temperature variations in the “swiveling zone” (point A) and in a point located at the core of the heel (point B).

Figure 15 shows a typical result of thermal fields recorded during repetition of impacts on a slanted heel. The heel temperature at the beginning of the test corresponded to the room temperature, i.e. 22.7°C. The temperature increased sharply at the beginning of the test because of the important irreversibility mechanisms involved in the impact and because of the weak heat conduction of the polymer. Then, due to the heat losses, the variations became less marked and a plateau appeared for many impacts. Temperature fields were recorded on the heel surface, so it is likely that heating was greater at the core of the structural component. For this type of heel, two heating zones were observed during repetition of the impacts. In the first one, i.e. the impact zone, marked temperature variations (about 18°C after 208 impacts) were mainly due to friction, viscoplasticity and damage mechanisms. The second one, which was critical for the structural component because it turned out to be the site of failure, was the “swiveling zone”, which was located at the bottom of the heel. Temperature variations here were about 12°C after 208 impacts.

The impact test is a critical experimental evaluation for the heel design. The objective of this study was to replace visual observations in real tests by a numerical model analysis in order to accelerate the design cycles and reduce costs.

Instrumentation of the machine was necessary to monitor and understand the test. We thus collected information during the impacts on: the force, velocities, global displacements, displacement and thermal fields. This experimental information was necessary to build and then validate the numerical model.

The thermal fields showed substantial temperature variations (more than 10°C at the surface) in the future failure zone. Previous experimental results obtained during tensile tests demonstrated that such temperature variations were not

negligible for the material. A test conducted at 40°C, compared to a lower one conducted at 27°C, led to a 4 MPa decrease for the yield stress σ_y . This indicated that thermal softening of the material should be taken into account. In order to approach a more realistic temperature distribution in the structural component, we also simultaneously attempted to solve the thermal problem in adiabatic conditions.

5. FINITE ELEMENT MODEL

Geometry

A presumably rigid clapper with a known angular velocity applied an impact on the heel model. The impact energy is a function of the inertia and angular velocity.

The two parts of the model, i.e. the clapper and heel, were obtained by CAD. The geometry of the clapper was simplified as compared to the real one. The striker was modeled by a perfect cylinder. In the case of the slanted heel, the geometry of the heel base was truncated to facilitate mesh generation and to avoid excessive distortion of the elements in this zone. Static elastic simulations have previously shown that stresses were weak in this zone. The geometry of the heels did not take into account the part embedded in the alloy. The heels were thus shortened a 10 mm height.

Mesh

Rigid shell elements were used for the external surfaces of the set clapper-striker (Figure 16). Solid elements, brick type with 8 nodes and reduced Gauss integration, were chosen for the heel. To optimize the time for computing, the density of the elements changed along the axis of the heel. There was a high density at the point of impact and in the "swiveling zone", a coarser mesh was applied in zones with a weak stress gradient. For the striker, the cylindrical end was the critical part and thus contained more elements than the remainder of the clapper.

The pins used to reinforce the slanted heels were made of steel (C60). They were developed starting from sheets which were folded to obtain the cylindrical form (Figure 17a), then quenched and tempered at 440 °C. On the pin surface, we noted some marks which increased the adhesion with the injected ABS polymer. Moreover, the pin was not a perfect cylinder, it had a split throughout its length. However, static elastic finite element simulation of a pin (split and not split), embedded at one extremity and subjected to a radial load at the other end, showed that the presence of the split was negligible for the end deflection (about 2% variation). Thereafter, in order to simplify the mesh, the pin was thus modeled by a cylinder without a split. A study to choose the type of elements (shell or solid) was carried out. Solid elements were selected (Figure 17b). An optimum of two elements in the thickness direction was obtained, which was a good trade-off between the accuracy and the computing time.

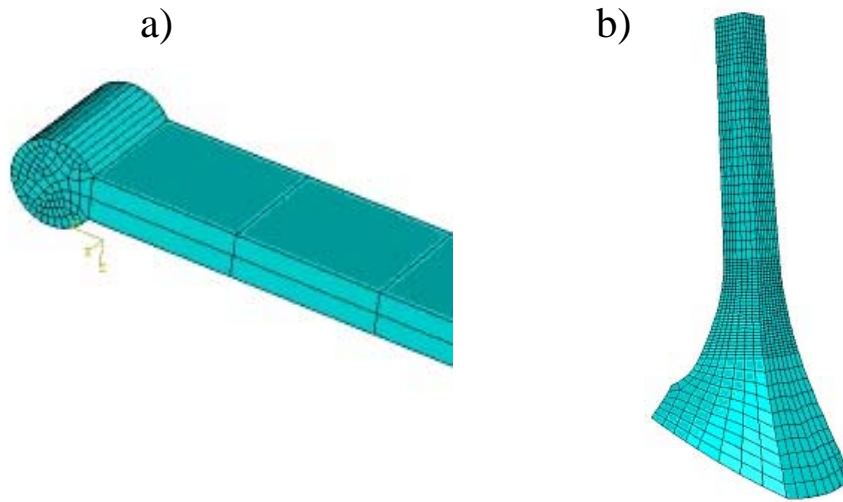


Figure 16: a) Clapper and striker mesh, b) slanted heel mesh (5000 elements)

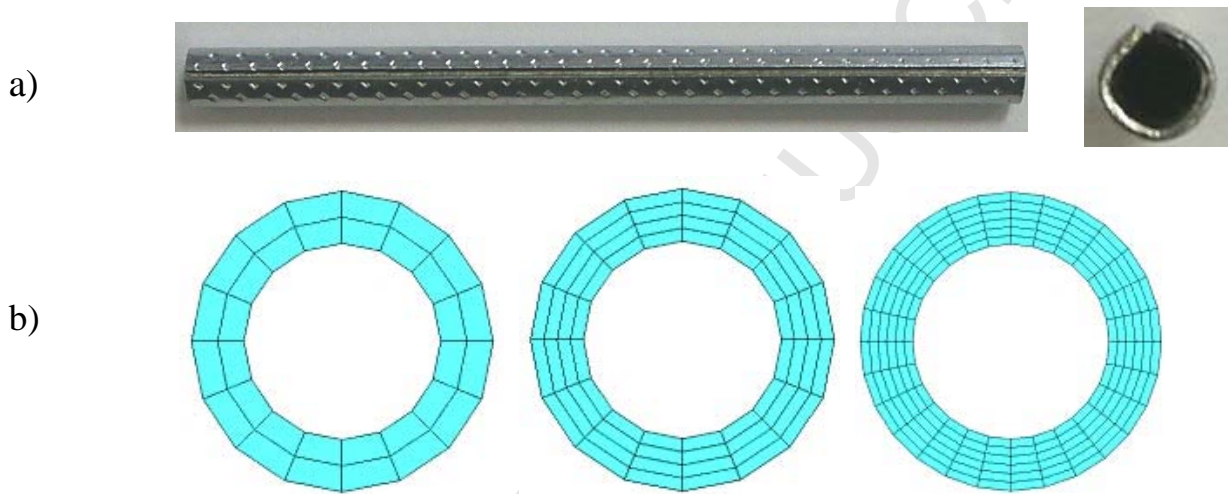


Figure 17: a) Radial and axial view of a pin. b) Mesh of the pin with a different number of elements in the thickness direction.

Initial and boundary conditions

In order to decrease the computing times, the impact was carried out in only one stage, i.e. the approach phase was not simulated. At $t=0$ s, the striker was positioned just before the impact, with an angle of 0.1° of the vertical position. Its angular velocity was determined before and controlled by a reference node with a nonzero value for its rotation degree of freedom and zero values for the others. The heel was embedded at its base. The duration of the simulated impact was 0.04 s.

6. RESULTS AND DISCUSSION

In this part, various simulations are presented: slanted heel without a reinforcement pin then with a pin. For each simulation, the results are discussed and compared with the experimental data.

Slanted heel without pin

The slanted heel did not support even one impact without a reinforcement pin. We thus simulated an impact at weaker energy, with a starting angle of 45° , with a speed and an energy identified according to the instrumentation of the machine. The heel was meshed with 8510 elements, the computing time for this simulation was about 2 h 20 min. Von Mises equivalent stresses are first presented (Figure 18a). Since they changed during the impact, they were plotted at the time when the force and displacement were maximal (time 0.018 s).

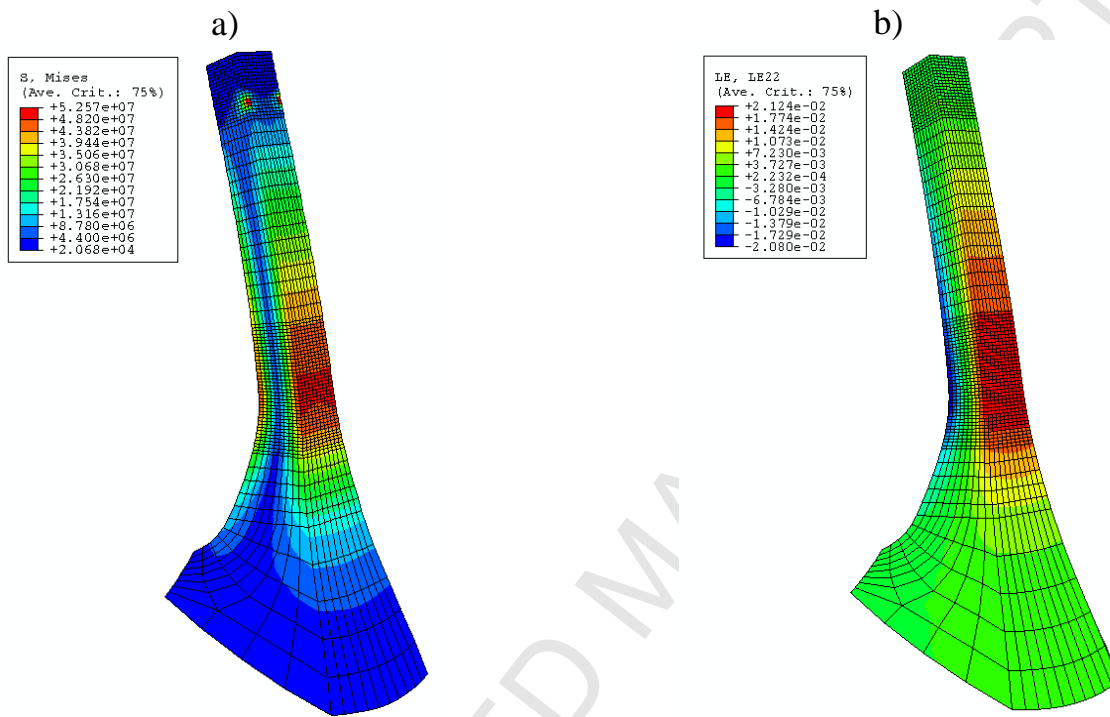


Figure 18: a) Von Mises equivalent stress (Pa) field given by the model. b) Axial component (in the heel direction) of the logarithmic strain.

Two zones of stress concentration appeared, one on the impact zone and the other on the "swiveling zone". Higher stresses were observed in the load application zone. The stress values reached in this zone were strongly dependent on the mesh density (52 MPa for the mesh presented). However, the behavior in this zone seemed to have little effect on the impact resistance of the structural component. The stresses remained low at the base of the heel. In the "swiveling zone", they reached 48 MPa. The yield stress of ABS, increased by the strain rate effect, was apparently not exceeded. This was checked by looking at the displacements obtained by the numerical model, where no permanent displacement was observed, as in the experiment (see Figure 19a).

The logarithmic strain according to the heel axis estimated by the model are plotted in Figure 18b. When submitted to bending loading, one side was loaded in traction and the other in compression, with maximum strain values of about 2%.

Monitoring displacement of the heel extremity in the impact direction enabled us to determine if there was permanent strain. This simulated value of the extremity displacement was compared with the measured value (Figure 19a). The displacement obtained by the simulation corresponded to the horizontal displacement of the heel, for a node located in the impact zone (5 mm from the heel tip). The curves highlighted a difference in the simulated and experimental impact duration: the time of simulated impact was shorter by more than 0.005 s. This 18% variation could be related to the uncertainty of the inertia determination obtained by a simplified CAD model of the clapper and/or to the fact that the damping of the base support of the heel was not taken into account. However, maximal displacements were well estimated. The boundary conditions related to the heel was a perfect embedding without damping, this choice could explain the oscillations observed on the figure after the impact. However, the average oscillation value was centered on the zero ordinate axis, which indicated that there were no permanent deformations of the material. Using the load sensor, it was also possible to compare the forces brought into play during the impact with those obtained by the simulation (Figure 19b). Simulated and experimental variations in the forces were close, with a difference between the modeling and experimental results of just 5%. The duration of the impact obtained by the simulation was slightly shorter than that of the real impact. Such a difference was already observed for the displacement.

The simulation of the heel without a pin gave results that agreed with the experimental findings. The impact carried out with such an angle was purely elastic, as observed experimentally. The displacement and force values corresponded to the experimental values. Nevertheless, there was still some variation between the simulated and experimental impact durations.

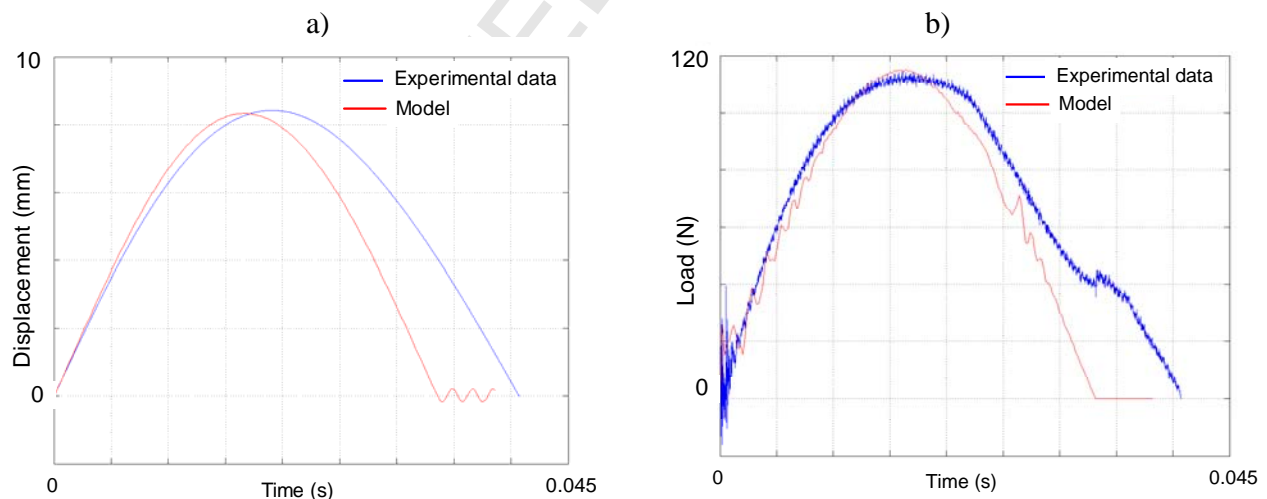


Figure 19: Model and experimental results for a 45° impact, on a slanted heel without a reinforcement pin. a)

Variations in the displacement of a point located at the heel extremity. b) Variations in load during the impact.

Slanted heel with pin

The Johnson Cook model described in section 3 was used for the heel structural component. The material model used for the pin was an elastoplastic law presented in the form of table in the finite element software. It was identified according to a tensile test which required a modified experimental setup. The yield stress of the pin material identified was 1000 MPa, with an uncertainty of approximately 50 MPa. During injection, the pin was completely embedded in the heel. Numerically, this characteristic was modeled by a solid-type embedded interaction.

Simulations were carried out for an impact with an initial orientation of 90° for the clapper. The maximum stress level was reached at time $t = 0.0082$ s, the results are presented for both the pin and heel (Figures 20a and 20b). The stress localization zones were located in the same places as the temperature localization zones. The stresses in the pin were high compared to those in the heel. The presence of the pin involved a shift in the "swiveling zone", which was located in a lower position than that of an impact on a heel without a pin. The pin seemed to support the entire impact. The yield stress of the latter was exceeded and there was unrecoverable deformation during the first impact, as observed in the experiments. The maximum stresses were reached in the same "swiveling zone" on the side loaded in traction. Because of the risk of creating and opening cracks during the repeated impacts, this zone was more critical than the compression zone. For the heel, the stress values reached 56 MPa, i.e. close to the yield stress at this strain rate. To determine whether the yield stress was reached, the levels of equivalent plastic strains available in the software were plotted (Figure 20c). These deformations were observed only on the pin, and no unrecoverable deformation was observed in the heel.

Simulated and measured displacements at the end of the heel are plotted on Figure 21a. The various experimental tests showed dispersion of the permanent displacement after the first impact. The average measured permanent displacement was 1.1 mm, with values ranging from 0.81 mm to 1.75 mm. The numerical simulation gave an average value of 1 mm, which closely agreed with the preceding experimental values. However, the maximum displacement was not correctly restored, higher displacement was obtained during the experiment. Figure 21b shows temporal variations in the impact load. Differences were observed between the load obtained by simulation and that obtained experimentally. The impact load found by simulation was weaker (variation of 100 N). This variation is in agreement with the observed displacements. The higher values for the measured impact load involved larger displacements. As for the simulation of the heel without pin, the duration of the simulated impact was shorter than in reality.

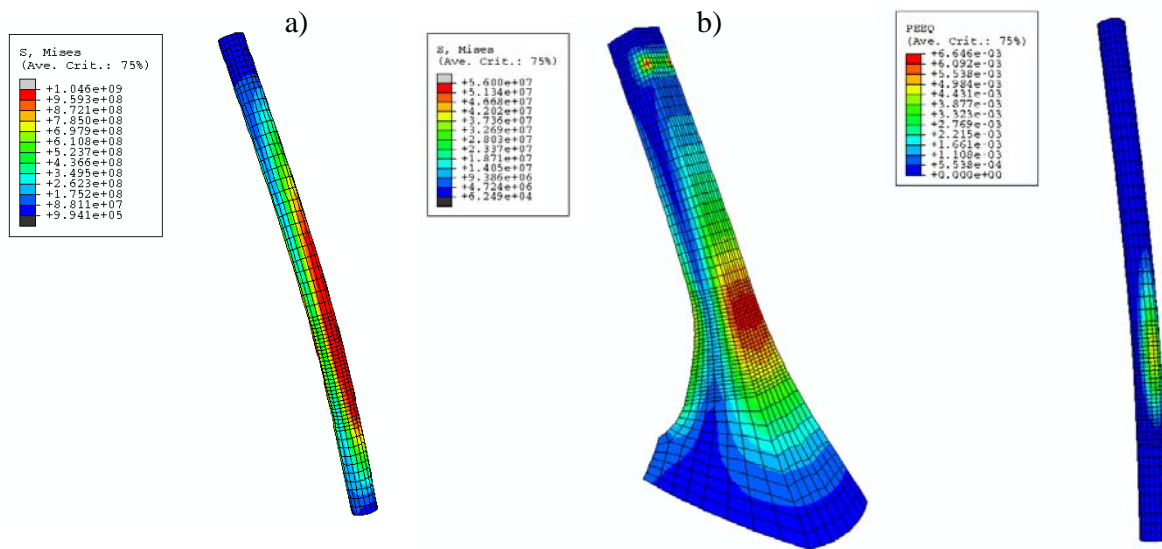


Figure 20: Model results for a 90° impact on a slanted heel with reinforcement pin. Equivalent Von Mises stresses: a) in the pin, b) in the heel. c) Axial logarithmic strains in the heel.

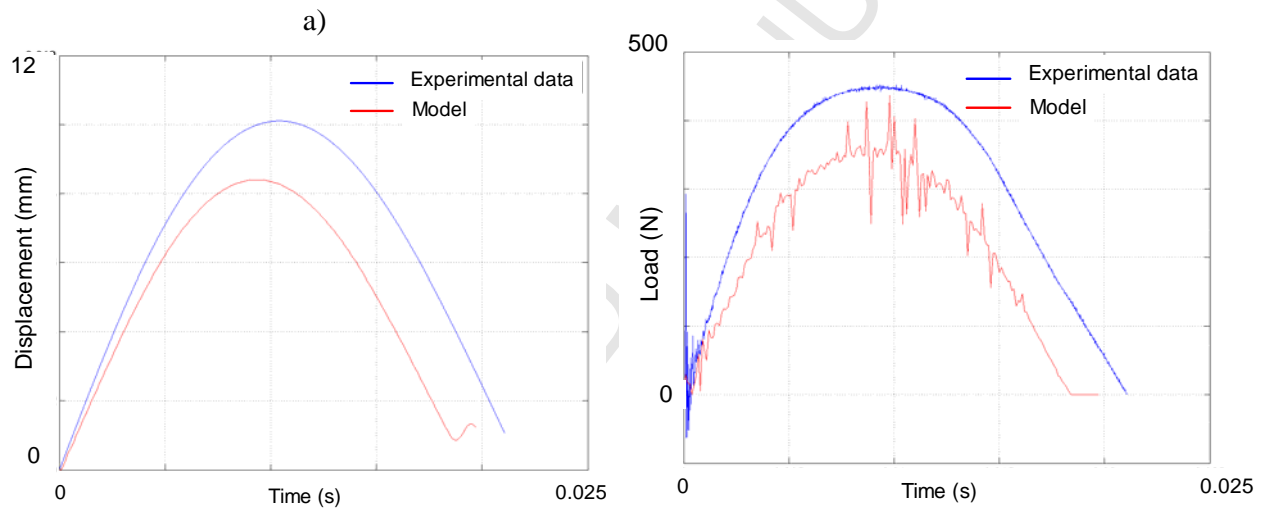


Figure 21: Model and experimental results for a 90° impact, on a slanted heel with reinforcement pin. a) Variations in the displacement of a point located at the extremity of the heel. b) Load variations during the impact.

Influence of friction

Temporal variations in the impact load given by the numerical model showed considerable noise. A study of sensitivity to the model parameters was carried out to determine the origin of these perturbations. The friction coefficient between the striker and the heel seemed to influence these fluctuations. The results, for an impact test with an initial clapper position at 90° on a slanted heel with a pin, are plotted in Figure 22. The curve oscillations increased with the friction coefficient. This study showed that the impact load values were not very influenced by the friction coefficient. Hereafter, an arbitrary coefficient of 0.1 will be used.

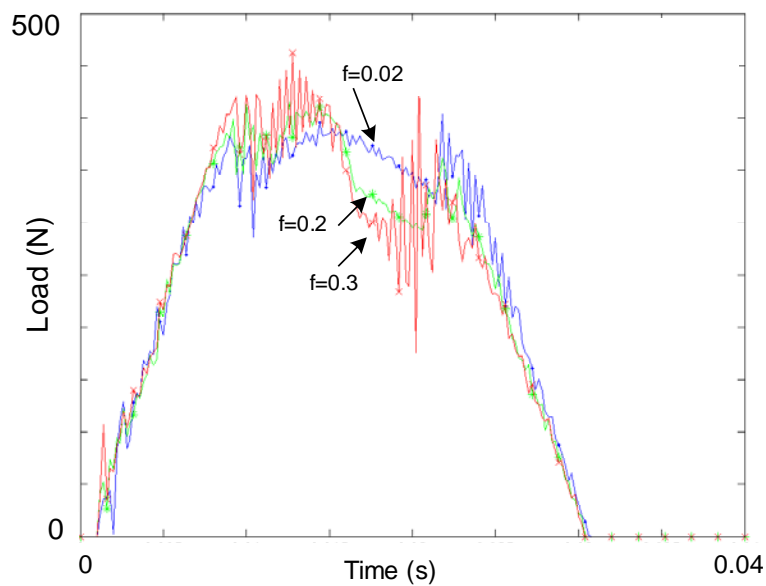


Figure 22: Friction coefficient influence on the impact load for a 90° impact on a slanted heel with a reinforcement pin.

7. CONCLUSION

The different development steps of a numerical model for an impact test on a slanted heel structural component are presented in this paper. This work was associated with a global project of time and cost reduction for heel shoe design studies. Preliminary experimental tensile and impact tests were conducted to observe the material and structural behavior. In these two situations, kinematics and thermal full field measurement techniques were used. With the kinematic fields, it was possible to identify the stress strain response, which takes the strain localization (necking) into account. Positive volume variations were also observed during these tensile tests, which were associated with the damage mechanisms of crazing in this type of polymer. The thermal fields measured during these tests showed marked temperature variations (a few K to 25 K) in the zone where the strain localization appeared. At the same time, the temperature variation fields recorded during a repeated impact test showed that marked temperature variations (18 K after 208 impacts) appeared in the "swiveling zone", which was the future zone of failure for the heel structural component. Temperature variations were due to possible irreversible mechanisms: viscosity, and/or plasticity, and/or damage. The associated thermal softening, estimated by the stress-strain response observations for various imposed room temperatures, was high and had to be taken into account in the material model. A Johnson Cook material model was selected because it can easily include the strain, strain rates and temperature effects. Its coefficients were identified using tensile tests at various strain rates and temperatures. In order to predict a more realistic decrease in yield stress due to thermal softening, a thermomechanical simulation was built. This weak coupled model assumed both the

adiabaticity of the problem and an estimation of the heat sources equaled to a fixed ratio (90%) of the local volume plastic power.

A finite element model of the impact test was then built using a commercial explicit finite element software. To validate the model, a specific instrumentation of the machine was carried out. It was thus possible to measure the displacements, linear and angular velocities and impact load. In addition to these local data, kinematics and thermal full field measurements were proposed and gave a rich spatiotemporal database to compare the experimental and numerical results. They supplied, at the surface of the structural component, displacement estimations and temperature variation fields.

Preliminary simulations on a notched sample were performed and compared with the experimental results to test the model in the simple tensile deformation mode. Global load-displacement responses and strain fields were in line with the experimental results. However, the calculated temperature variations were underestimated. This difference could be attributed to the absence of damage, which was strongly dissipative, in the material model. Simulations, on a slanted heel without a pin, of a weak energy impact test with an initial clapper angle position of 45° , were then carried out. The results closely agreed with the experimental data. Then simulations on a heel reinforced by a pin submitted to an impact test at the nominal measured energy of 1.61 J (corresponding to an initial angle position of 90°) were performed. An underestimation about 20% of the impact load was obtained by the model. A study of sensitivity of the heel and pin geometry, of the elastic properties of the ABS and the steel of the pin, and of the friction coefficient between the striker and the heel showed that the influence of these parameters on the results was less than 5%. Other causes could explain this difference. The first one could be a difference in the ABS material between the heel structural component and the tensile samples used for material identification, which was due to different process parameters during manufacturing by injection. The others could be (i) the aging of the material, (ii) the identification of the material based only on uniaxial tensile tests and the (iii) Mises yield surface used in the Johnson Cook Model. Future experiments, including compression and/or shear tests, on this material could improve the material model. In particular, it could be interesting to use (or implement) other types of models, such as damage models or Drucker-Prager model well adapted to pressure sensitivity of ABS materials [14].

Acknowledgement

The support of the LMOPS laboratory (Université de Savoie – France), particularly Patrice Mélé, for carrying out the high-speed tensile test is gratefully acknowledged.

REFERENCES

1. Socrate S, Boyce MC, Lazzeri A. A micromechanical model for multiple crazing in high impact polystyrene. *Mech Mat* 2001; 33:155-175.

2. Ramsteiner F, Heckmann W, Mckee GE, Breulmann M. Influence of void formation on impact toughness in rubber modified styrenic-polymers. *Polymer* 2002; 43:5995-6003.
3. Seelig T, Van Der Giessen E. Localized plastic deformation in ternary polymer blends. *Int J Solids Struct* 2002; 39:3505-3522.
4. Rittel D. On the conversion of plastic work to heat during high strain rate deformation of glassy polymers. *Mech Mat* 1999;31:131-139.
5. Fond C, G'Sell C. Localisation des déformations et mécanismes d'endommagements dans les polymères multiphasés. *Méca Indust* 2002 ;3, :431-438.
6. G'Sell C, Hiver JM, Dahoun A. Experimental characterization of deformation damage in solid polymers under tension, and its interrelation with necking. *Int J Solids Struct*. 2002;39:3857-3872.
7. Wattrisse B, Muracciole JM, Chrysochoos A. Thermomechanical effects accompanying the localized necking of semi-crystalline polymers. *Int J Therm Sci* 2002 ;41:422-427.
8. Billon N. Effet de couplage thermomécanique dans la caractérisation du comportement de polymères solides. *Méca Indust* 2003 ;4:357-364.
9. Cros PE, Rota L, Cottenot CE, Schirrer R, Fond C. Experimental study and numerical simulations of the impact behaviour of polycarbonate and polyurethane multilayer. *J Phys IV France* 2000;10:671-676.
10. Duan Y, Saigal A, Grief R, Zimmermann MA. A uniform phenomenological constitutive model for glassy and semicrystalline polymers. *Pol Eng Sci* 2001;41(8):1322-1328.
11. Duan Y, Saigal A, Grief R, Zimmermann MA. Analysis of multiaxial impact behaviour of polymers. *Pol Eng Sci* 2002;42(2):395-402.
12. Duan Y, Saigal A, Grief R, Zimmermann MA. Impact behavior and modeling of engineering polymers, *Pol Eng Sci* 2003;43(1):112-124.
13. Dean G, Read B. Modelling the behaviour of plastics for design under impact. *Pol Test* 2001;20:677-683.
14. Dean G, Wright L. An evaluation of the use of finite element analysis for predicting the deformation of plastics under impact loading. *Pol Test* 2003;22:625-631.
15. Piette-Coudol F. Modélisation et simulation de la tenue aux chocs des talons de chaussure femme. PhD Thesis, Université de Savoie, France, 2006.
16. Vacher P, Dumoulin S, Morestin F, Mguil-Touchal S. Bidimensional deformation measurement using digital images. *Proc Instn Mech Engrs* 1999;213(C):811-817.
17. Coudert T. Reconstruction tridimensionnelle du volume intérieur d'une chaussure, évaluation du chaussant. PhD Thesis, Université de Savoie, France, 2005.
18. Tabourot L, Vacher P, Coudert T, Toussaint F, Arrieux R. Numerical determination of strain localization during finite element simulation of deep drawing operations. *J Mat Proc Tech* 2005 ;159(2):152-158.
19. Chrysochoos A, Louche H. An Infrared image processing to analyse the calorific effects accompanying strain localisation. *Int J Eng Sci* 2000;38:1759-1788.
20. Seidler S, Grellmann W. Application of the Instrumented Impact Test to the Toughness Characterization of High Impact Thermoplastics. *Polymer Testing* 1995;14:453-469.

21. Grellmann W, Seidler S, Hesse W. Testing of plastics, instrumented Charpy impact test. MPK Procedure. http://www.iw.uni-halle.de/ww/mpk/p_e.pdf, 2007.

Lorriot T, Martin E, Quenisset JM, Rebiere JP. Dynamic analysis of instrumented Charpy impact tests using specimen deflection measurement and mass-spring models. *Int J Fract* 1998;91:299-309.

ACCEPTED MANUSCRIPT

Figure Captions

Figure 1: Global mechanical response for: a) various strain rates ($V_1=2 \text{ s}^{-1}$, $V_2=1 \text{ s}^{-1}$, $V_3=0.2 \text{ s}^{-1}$, $V_4=3.10^{-2} \text{ s}^{-1}$, $V_5=1.10^{-2} \text{ s}^{-1}$, $V_6=1.10^{-3} \text{ s}^{-1}$), b) various imposed ambient temperatures ($T_1=40^\circ\text{C}$, $T_2=50^\circ\text{C}$, $T_3=60^\circ\text{C}$), at 0.1 s^{-1} . c) Yield stress vs. strain rates, for various imposed room temperatures ($T_1=27^\circ\text{C}$, $T_2=40^\circ\text{C}$, $T_3=50^\circ\text{C}$, $T_4=60^\circ\text{C}$).

Figure 2: a) Photograph of the sample with the virtual grid, the position of the three local points and the virtual extensometer, b) logarithmic axial strain field ε_{11} observed for a global displacement of 9 mm, at a strain rate of 8.10^{-4} s^{-1} , c) Local response (true strain and true stress) obtained in the three different points of Figure a). The mean axial strain given by the extensometer is 0.09, instead of the local value of 0.65 given by the strain field analysis.

Figure 3: a) Volume variation measured during a tensile test at 8.10^{-4} s^{-1} , b) Stress strain responses, for the three hypotheses, at a strain rate of 8.10^{-3} s^{-1} .

Figure 4: a) Thermal field, at a fixed time ($t=2\text{s}$, see Figure b), observed during a tensile test at a strain rate of $4.5.10^{-2} \text{ s}^{-1}$, showing a localization at the bottom of the sample (point 1). b) Temporal variations in the temperature at the three spatial points of the previous figure. The high temperature jump ($+26^\circ\text{C}$) observed at point 1, at time 4.3 s, is associated with intense dissipation in the necking zone during failure. In the two other points, the temperature increase is mainly due to thermoelasticity linked to elastic spring back.

Figure 5: Identification of the Johnson Cook model. Comparison of the stress-strain response given by the model and by the experimental results for two imposed strain rates: a) 10^{-3} s^{-1} , b) 3.10^{-2} s^{-1} .

Figure 6: a) Geometry of the notched specimen. b) Global view of the mesh. c) Close-up of the mesh in the notched part. d) Comparison of the model and experimental results, under imposed strain rate (4.10^{-2} s^{-1}) and room temperature (27°C) conditions.

Figure 7: a) Digital image of the notched zone, with the virtual grid used in the 7D[®] DIC software. b) Experimental and c) simulated fields of the axial logarithmic strain in the notched zone.

Figure 8: Tensile test at 2.10^{-2} s^{-1} . a) Temperature field measured in the notched zone, just before failure. b) Axial and transverse temperature profile (central column and central line of the previous figure)

Figure 9: Temperature variations (K) calculated by the Johnson Cook model during a tensile test on a notched specimen.

Figure 10: a) Pendulum impact test machine, b) Scheme of the support and load conditions applied to the heel structural component.

Figure 11: a) Scheme of temporal variations in loading. b) Slanted heel structural component embedded in a low melting point alloy.

Figure 12: Instrumentation of the machine. a) close-up showing the load sensor used to measure the impact force. b) Close-up of the gyroscope, fixed in the clapper, used to measure its angular velocity. c) Impact load response measured during an impact test at 90° on a slanted heel with a pin.

Figure 13: Digital images used by the DIC software to estimate displacements at the end of the structural component: a) initial state, b) after 140 impacts, with an indication of the measured displacement.

Figure 14: a) Variations, with the number of repeated impacts, in the permanent displacement measured at the end of the structural component; the 10 curves are associated with the 10 heels tested. b) Permanent displacement after the first impact, for the different tests.

Figure 15: Temperature field measurement in a slanted heel. a) Temperature field after 208 impacts. b) Temperature variations in the “swiveling zone” (point A) and in a point located at the core of the heel (point B).

Figure 16: a) Clapper and striker mesh, b) slanted heel mesh (5000 elements)

Figure 17: a) Radial and axial view of a pin. b) Mesh of the pin with a different number of elements in the thickness direction.

Figure 18: a) Von Mises equivalent stress (Pa) field given by the model. b) Axial component (in the heel direction) of the logarithmic strain.

Figure 19: Model and experimental results for a 45° impact, on a slanted heel without a reinforcement pin. a) Variations in the displacement of a point located at the heel extremity. b) Variations in load during the impact.

Figure 20: Model results for a 90° impact on a slanted heel with reinforcement pin. Equivalent Von Mises stresses: a) in the pin, b) in the heel. c) Axial logarithmic strains in the heel.

Figure 21: Model and experimental results for a 90° impact, on a slanted heel with reinforcement pin. a) Variations in the displacement of a point located at the extremity of the heel. b) Load variations during the impact.

Figure 22: Friction coefficient influence on the impact load for a 90° impact on a slanted heel with a reinforcement pin.

Tables

Table 1 – Identified values of the Johnson Cook model parameters